Applied Surface Science 473 (2019) 156–163

Contents lists available at ScienceDirect

Applied Surface Science

journal homepage: www.elsevier.com/locate/apsusc

Full Length Article

Graphitic coated Al nanoparticles manufactured as superior energetic materials via laser ablation synthesis in organic solvents

Seyyed Ali Davari[a,b], Jennifer L. Gottfried[c,*], C. Liu[e], Erick L. Ribeiro[d,f], Gerd Duscher[e], Dibyendu Mukherjee[a,d,f,*]

[a] Department of Mechanical, Aerospace, & Biomedical Engineering, University of Tennessee, Knoxville, TN 37996, USA
[b] Department of Mechanical and Aerospace Engineering, Air Quality Research Center (AQRC), University of California Davis, 2132C Bainer Hall, One Shields Ave, Davis, CA 95616, USA
[c] RDRL-WML-B, US Army Research Laboratory, Aberdeen Proving Ground, MD 21005, USA
[d] Department of Chemical & Biomolecular Engineering, University of Tennessee, Knoxville, TN 37996, USA
[e] Department of Material Science and Engineering, University of Tennessee, Knoxville, TN, USA
[f] Nano-BioMaterials Laboratory for Energy, Energetics & Environment (nbml-E^3), University of Tennessee, Knoxville, TN 37996, USA

ARTICLE INFO

Keywords:
Laser ablation synthesis in solution (LASiS)
Organic solvents
Graphitic shell
Aluminum nanoparticles
Energetic nanocomposites

ABSTRACT

The large heat release predicted in the early investigations of energetic aluminum nanoparticles (Al NPs) used in solid-state propulsion and pyrotechnics has been offset by hindered diffusion-limited detonation rates due to excess oxide shell formations and surface area loss from aggregations. We address these challenges by manufacturing graphitic shell coated Al NPs (< 20 nm sizes) via laser ablation synthesis in solution (LASiS) to preserve high surface areas and interfacial properties of Al NPs. Specifically, we use a high-energy laser to ablate Al pellets confined in either acetone or toluene to coat the laser-ablated Al NPs with graphitic shells generated from the thermal pyrolysis of the organic solvents. Energetic activities of the C/Al NPs were tested via the laser-induced air shock from energetic materials (LASEM) technique. We demonstrate that synthesis parameters such as organic solvents, laser flux and ablation times can be tuned to provide superior control of NP sizes/aggregation with the aid of the C shell formations and, in turn, their energetic behavior. This study unveils the synthesis-structure-property relations in LASiS-based manufacturing of energetic nanocapsules within graphitic shells that are safe to handle and can undergo kinetically controlled spontaneous energy release under desired conditions.

1. Introduction

The last few decades have seen a large volume of research work focus on a class of novel metallic materials that demonstrate enhanced energetic properties, thereby finding applications as propellants, explosives and pyrotechnics [1,2]. To this end, past studies involving different mixtures of aluminum (Al) powders and oxidizers as heterogeneous, composite solid propellants have demonstrated high burning rates and enhanced ignition [3–6]. A substantially larger surface area arising from fuel-oxidizer interfaces in the nanoscale regime promotes the kinetically controlled ignition processes. In this regard, the early investigations of energetic nanomaterials primarily focused on the use of metal nanoparticles (NPs), especially nano-Al, in explosives [7–12]. The energetic behavior in these materials is largely driven by the excess interfacial area and small diffusion length scales. In fact, notable works in the past [9,13] have analyzed the unique combustion properties of various energetic materials at nano-scale as compared to their properties at micro-scale. Studies of the heterogeneous combustion characteristics of various nano-powders and nano-composites of explosive materials like ammonium nitrite, cyclotrimethylene trinitramine (RDX), and Al have also been carried out [14]. Such interests have obviously arisen from the increasing need for reliable alternative sources of solid fuel additives and propellants for the ever-expanding and critical defense and aerospace applications.

The combustibility and reactivity of Al particles have been of considerable research interest due to the large negative enthalpy of combustion for Al (e.g., for bulk Al, $\Delta H_B = -1675$ kJ/mol and for a single Al atom, $\Delta H_1 = -2324$ kJ/mol). The difference in enthalpy between bulk and atomic Al has been attributed to the differences in the kinetics of bulk and nanosized particles [2]. Although extensive studies have looked into the gas phase oxidation of micron-sized Al particles in the continuum regime [15], it is obvious from these studies that the criteria

* Corresponding authors at: Department of Mechanical, Aerospace, & Biomedical Engineering, University of Tennessee, Knoxville, TN 37996, USA.
E-mail addresses: jennifer.l.gottfried.civ@mail.mil (J.L. Gottfried), dmukherj@utk.edu (D. Mukherjee).

https://doi.org/10.1016/j.apsusc.2018.11.238
Received 14 September 2018; Received in revised form 21 November 2018; Accepted 29 November 2018
Available online 01 December 2018
0169-4332/

for continuum burning (where particle size is significantly larger than mean free path of the gas) cannot be extended to ultra-fine metal particles (< 100 nm) [12]. Al NP oxidation and its energy release can be described by several mechanisms related to the transport of the participating reactive species and surface reactions, namely: (1) reaction between the background O_2 and the surface Al atoms; (2) formation of oxide layer on the surface Al; (3) diffusion of O_2 and Al through the oxide layer for subsequent reactions. It has been shown that the morphology of the particles, especially the oxide layer thicknesses, changes the energetic properties of Al NPs drastically [16]. The formation of the native oxide layer affects the surface reactivity and oxidation kinetics of Al NPs significantly, as the reaction mechanism proceeds from reaction-limited kinetics at the initial stages on the bare Al surface to a diffusion-limited regime once the reactive species have to diffuse through the pre-formed oxide shell [16]. Therefore, it could be beneficial to design energetic NPs with optimal oxide shells to passivate the Al NP surface for safety reasons, or to tune their surface oxidation rates. Increasing efforts in the design of next-generation energetic nanomaterials have been directed towards the basic idea that the coatings should not simply retard the reactivity, but promote safety while simultaneously enabling performance enhancement. Hence, various scenarios have been suggested to preserve the surface reactivities by using noble metals [17], metal oxides [18] and other potent oxidizers [18–20] to coat the active metal NP. The use of oxidizing agents as the coating on metal NPs also reduces the solid fuel-oxidizer diffusion lengths, thereby promoting the burning rates [21]. Carbon coatings have been demonstrated to show similar features [22], with the added advantage that while the coating itself gets oxidized into gaseous products (CO_2, CO etc.) to prevent any solid ash residues on the particle surface, the Al NP aggregation rates are retarded due to the presence of the carbon shell.

The lab-scale and industrial synthesis of metal NPs typically employ rapid condensation of supersaturated metal vapor (monomers) generated from thermal evaporation of the bulk metal, electric arc discharge, laser ablation, flame reactors, or plasma reactors. Numerous theoretical studies have investigated the formation of Al NPs during gas phase synthesis [23–26]. However, it quickly became apparent that a significant drawback of gas-phase synthesis of metal NPs results from the kinetics of the process, which leads to high particle collision-coalescence rates, rapid aggregation, and loss of interfacial activities. On the other hand, chemical synthesis routes are powerful and have been extensively used to-date. However, they inevitably suffer from harsh residual chemical contaminations and equilibrium growth pathways for the particles, while requiring the use of unwanted surfactants and ligands during the synthesis [27].

Laser ablation techniques are of great interest in synthesis [28–31] and characterization [32–36]. In this regard, laser ablation synthesis in solution (LASiS) has been considered as a “green chemistry” route that does not involve the use of surfactants and harsh reducing agents that typically poison the active surface areas. Previous studies on LASiS [37–45] have extensively developed the technique as a simple, versatile, and chemically clean approach to synthesize wide classes of metal/intermetallic nanoparticles. Moreover, from the industrial perspective, this technique is more economical for facile, rapid and large-scale production as compared to wet chemistry techniques [27]. Our recent series of studies on LASiS has shown that by tuning laser energy, wavelength, target metals of choice, solution chemistry, etc., various nanostructures such as binary nanoalloys, nanocomposites [46–48], ternary nanoalloys [49,50], and 2D materials [51] can be produced with different size, morphology, surface coatings, and chemical compositions. Conventional laser ablation has been employed in the past for the production of bare Al NPs [52]. A few studies have also looked into the size and morphology of Al NPs made from Al target ablation in organic solution [53,54]. Uncertainties in size, morphology, and structure of the Al NPs prevented further development of the technique into reliable and tunable systems that can effectively tailor the surface functionalities and/or coatings on the synthesized NPs. In fact, a vast majority of these studies have largely focused on the mere synthesis of these materials, and are devoid of any comprehensive investigations into tuning the energetic and other surface functional activities of these materials through systematic coatings to preserve solid Al fuel cores and prevent them from unwanted surface oxidation.

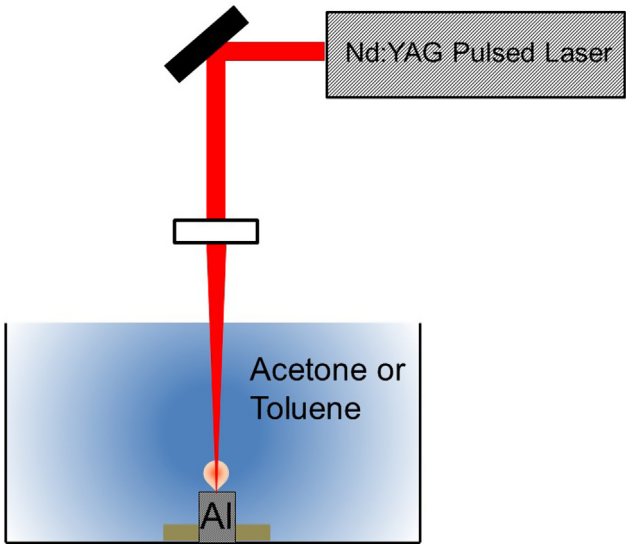

Fig. 1. Schematic for the in-house developed LASiS set-up.

In this paper, we present a facile yet rapid route to synthesize Al NPs with carbon/graphitic coatings as energetic nanomaterials by using LASiS with different organic solvents (acetone, toluene) and laser properties. The size/morphology, interfacial structures, and compositions of the shell-core C/Al NPs have been analyzed in light of their energetic performance as compared to various samples made under different experimental conditions, as well as with commercial native oxide-shell coated nanometer-sized Al powders.

2. Experimental procedure

2.1. LASiS set-up

The LASiS experimental set-up is illustrated in Fig. 1. A Q-switched Nd-YAG pulsed laser operating at 1064 nm with 4 ns pulse width, 10 Hz repetition rate and maximum energy 330 mJ/pulse is used for ablating the target in the cell. The cell is provided with two side-viewing windows to monitor and adjust the laser focal point. A gas inlet and an outlet on the cell allows for suitable purging with inert gases if needed. The Al target is mounted on a stepper motor and rotates continuously to enable uniform ablation from the surface. The reactor cell is also equipped with heating rods, a thermocouple for accurate monitoring of solution temperature, and a sonic dismembrator for in-situ de-agglomeration of the synthesized NPs.

2.2. Synthesis of Al NPs

The Al pellet was purchased from Kurt J. Lesker (99.99% purity, 1″ diameter and 1/4″ height). Two different organic solvents from Sigma-Aldrich (acetone, 99.95% purity and toluene, 99.9% purity) were used in this study for ablation of Al in solution. The Al target was placed in ~8 ml of the organic solvent and ablated with the laser at room temperature. Following laser ablation, the NP suspensions in the organic solvents were centrifuged, decanted and washed with methanol prior to deposition on the TEM grids for imaging, while the dried powder stored under an inert environment was used for all other characterization purposes. Commercial Al NPs (80 nm) were purchased (NovaCentrix) for comparison to the LASiS-synthesized particles.

2.3. Laser-induced air shock from energetic materials (LASEM)

Recently a new technique for measuring the microsecond-timescale energy release of residue materials, laser-induced air shock from energetic materials (LASEM), has been developed in order to estimate the energetic properties of exothermic and explosive materials [55–57]. Briefly, a shock wave is generated in the air above the sample using a focused Nd:YAG laser pulse (1064 nm, 6-ns, 850 mJ) to create a laser-induced plasma on the sample surface. Schlieren imaging with a high-speed camera is subsequently used to track the expansion of the laser-induced shock wave; the measured velocity of the laser-induced shock wave is indicative of the extent of the energy release on the microsecond timescale. For conventional military explosives, a strong correlation between the characteristic laser-induced shock velocity of the material and the measured detonation velocities from large-scale testing was observed. In this work, all LASEM analyses for the as-synthesized and commercial NPs have been carried out at the U.S. Army Research Laboratory facilities. The LASEM samples were prepared by spreading the dry powder in a thin residue affixed to double-sided tape. Excess material not embedded in the tape was ejected away from the sample surface by the laser-induced shock wave and did not chemically react in the laser-induced plasma.

3. Results and discussion

3.1. Structural characterization

Fig. 2 illustrates the STEM images for the NPs generated from the ablation of the Al pellets for 4 min under either acetone or toluene at a laser fluence of 2.6 J/cm^2; HRTEM images for individual particles prepared in acetone or toluene are also shown. For both solvents, the LASiS-synthesized samples consist of Al NPs embedded in a carbon matrix. Fig. 3 illustrates the Raman spectra for samples prepared in either acetone or toluene. It shows that both samples include the D (defect) and G (graphitic) bands at ~1375 and 1585 cm^{-1}, respectively. The observation of D and G bands suggest the presence of amorphous carbon and graphitic structures in both samples. It is noted

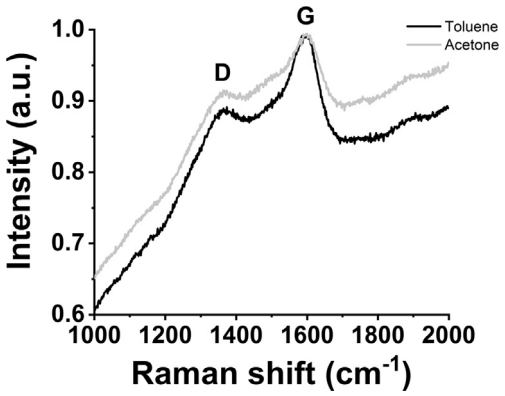

Fig. 3. Raman spectra for the samples prepared in acetone or toluene; labels indicate the well-known D and G bands for carbon.

that the presence of D band stems from the incomplete formation of graphitic shells and/or the amorphous carbon matrix shown in Fig. 2. For detailed investigation of the interfacial structures of the as-produced C/Al composite NPs, electron energy loss spectroscopy (EELS) has been used to analyze the morphology of the particles (Fig. 4). Here, it can be observed that for the synthesis in acetone, the Al NP has been covered with a graphitic shell coating. Moreover, the elemental distribution analysis across the dotted line shown in Fig. 4d confirms the core-shell structure by revealing a carbon-rich shell and central Al core. EELS measurements (shown in Supplementary Information, Fig. S1) for the samples prepared in toluene also revealed nanostructures consisting of Al cores with graphitic shells, although the cores were more crystalline than the samples produced in acetone. Current investigations are underway in our group to further elucidate the detailed structure-composition analysis of the core-shell nanostructures synthesized under different organic solvents.

Supplementary data associated with this article can be found, in the online version, at https://doi.org/10.1016/j.apsusc.2018.11.238.

By comparing Fig. 2a and b, one can immediately observe that the ablation in toluene resulted in larger particles as compared to the

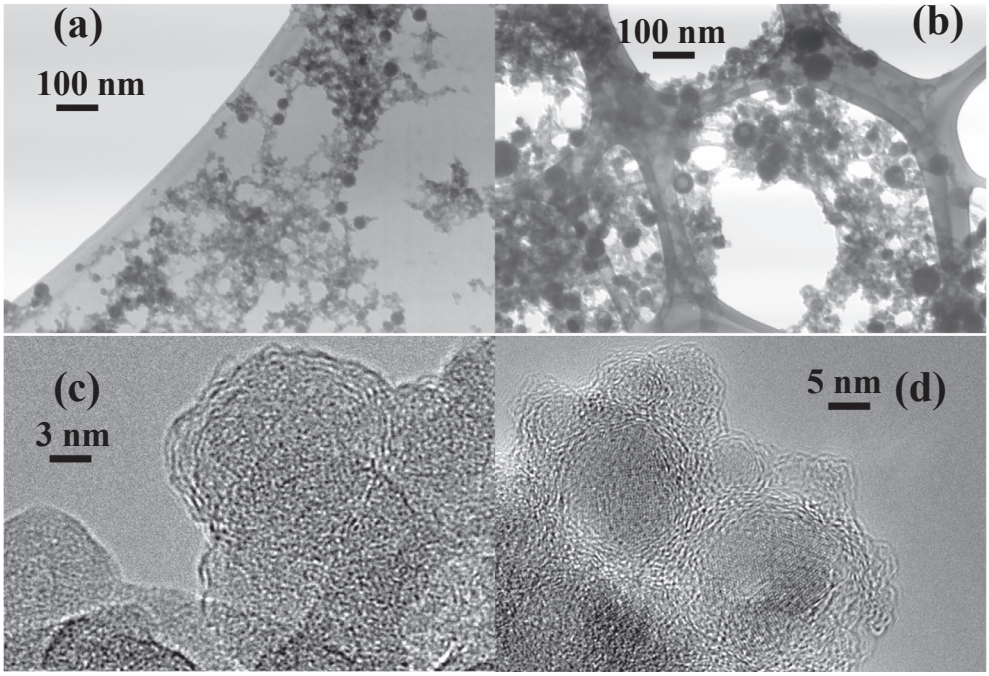

Fig. 2. Scanning transmission electron microscope (STEM) images of composite C/Al NP samples prepared via LASiS in (a) acetone and (b) toluene. High-resolution transmission electron microscope (HRTEM) images of composite C/Al NP samples prepared via LASiS in (c) acetone and (d) toluene.

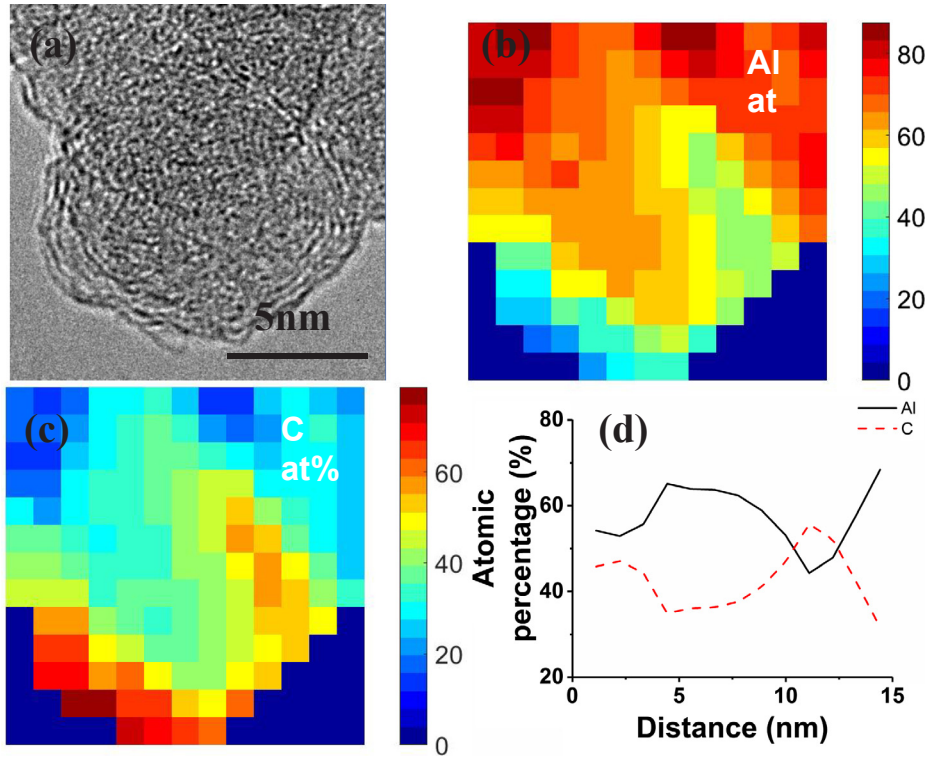

Fig. 4. (a) HRTEM image of the Al/C composite prepared in acetone indicating graphitic shell coatings on the Al NP core. EELS elemental mapping for the corresponding species (b) Al or (c) C. The atomic ratio (%) distributions for Al (solid black line) and C (dashed red line) across the line scan are shown in (d).

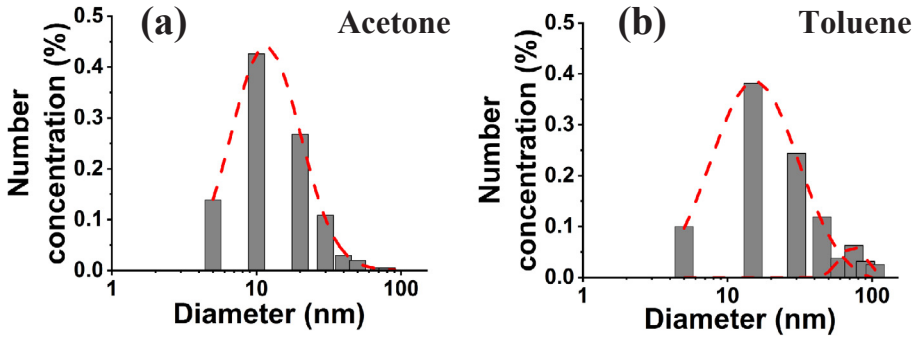

Fig. 5. Effect of organic solvents on the size distributions of the C/Al NPs prepared in (a) acetone and (b) toluene for ablation at a laser fluence of 2.6 J/cm^2 for 4 min.

samples from the ablation in acetone. To confirm these visual observations, the particle size distributions for both cases were analyzed. Fig. 5 shows the size distribution of the particles synthesized in acetone and toluene at a laser fluence of 2.6 J/cm^2 for 4 min. Both samples indicate a lognormal distribution. Based on the size distribution, it can be observed that the samples synthesized in acetone show a unimodal distribution with the peak value at 15.7 nm (log-normal standard deviation of σ = 11.0 nm). On the other hand, the samples synthesized in toluene indicate a bimodal distribution with a major peak at 25 nm (σ = 25.3 nm) and a minor one at 77.2 nm (σ = 17.2 nm). These results could be explained in relation to the distinct vapor pressure (V.P.) differences between acetone (V.P. ~32 kPa) and toluene (V.P. ~3.8 kPa). Particle growth is governed by the nucleation of Al monomers in the plasma-cavitation bubble, which leads to the formation of the primary particles. In general, these primary particles are released into the solution once the cavitation bubble collapses [27,58,59]; they then experience further growth due to coagulation and Al-Al collisions. However, the presence of amorphous carbon produced by the pyrolysis of organic solvents retards the collisions between Al particles and, subsequently, further growth of the Al nanoparticles. Since the vapor pressure of acetone is ~1 order of magnitude greater than toluene, more carbon will be produced due to pyrolysis of organic solvent. Hence, from a simple reaction kinetics analysis where the number of collisions between C and Al particles $N_{carbon-Al} = k_{carbon-Al} n_c n_{Al}$ such that $k_{carbon\text{-}Al}$ is the free molecular collision kernel for the C and Al monomer concentrations n_c and n_{Al}, respectively, $N_{carbon\text{-}Al}$ will be greater in acetone as compared to toluene (i.e., n_c will be larger for acetone). This proposed route of retardation in Al aggregation due to enhanced pyrolysis is also supported by the smaller particle sizes as well as the lower standard deviation in the particle size distribution obtained from acetone.

The effect of ablation time on the particles size distribution has been investigated for the samples in toluene. Fig. 6 shows the particle size distributions obtained for the Al pellets ablated in toluene for 2, 4, 6, and 8 mins at 2 J/cm^2 laser fluence. Here, the size distribution shows a bimodal behavior. As the laser ablation time increases from 2 min to 8 min, the first peak becomes wider (σ = 10.7 nm for 2 min and σ = 18.1 nm for 8 min). Moreover, the second peak at 2 min (~77 nm) shifts to smaller particles at 8 min (~25 nm) as its intensity correspondingly increases. The observation indicates that as the ablation

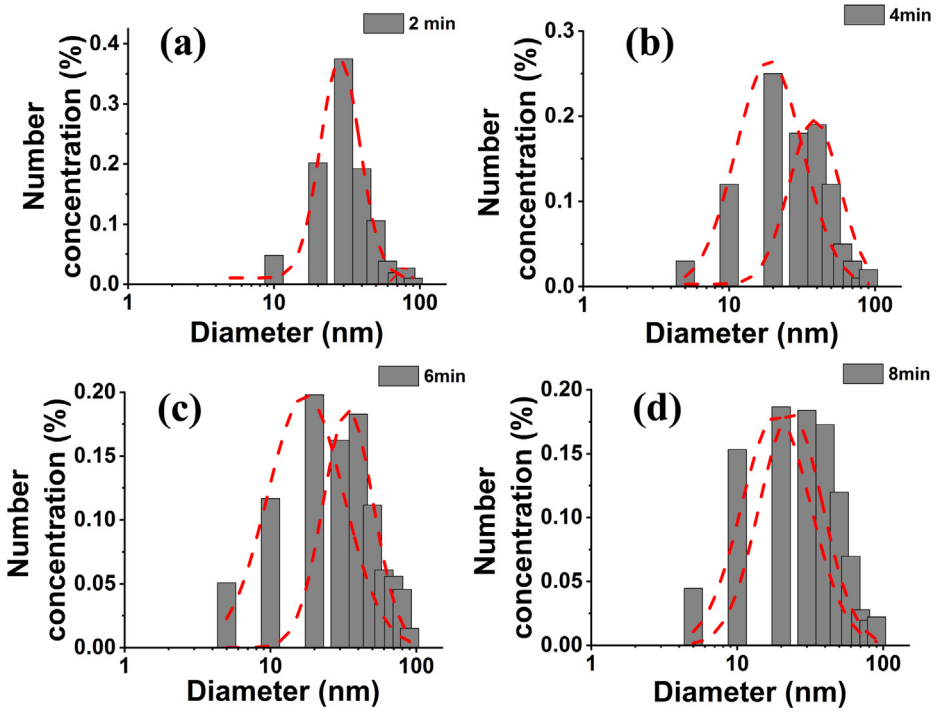

Fig. 6. Effect of laser ablation time on size distribution of the C/Al NPs prepared from LASiS in toluene at 2 J/cm laser fluence.

time increases, the difference between the first and second peaks in terms of the modal size and concentration decreases. Upon considering the free molecular collision kernel for the suspended particles in the solution: $k_{particles}\sqrt{T_{Solution}}$, where $T_{solution}$ represents the solution temperature, one can easily observe that the particle size distribution evolution as a function of the ablation time can be explained by the increase in the solvent temperature and thermal stresses which, in turn, promote aggregation and sintering of the particles.

Further investigations have been carried out on the effect of laser fluence on the particles size distributions. Fig. 7 illustrates the particle size distributions from Al targets ablated in acetone and toluene at 2.6 and 10.5 J/cm^2 laser influences for 4 min. In both the cases, one observes that as the laser fluence increases, the NP modal sizes and the standard deviations become smaller. In the case of acetone, the distribution peak of 15.7 nm (σ = 11.0 nm) at the laser influence of 2.6 J/cm^2 reduces to 12.3 nm (σ = 6.3 nm) at 10.5 J/cm^2. The same results can be seen in toluene wherein a bimodal distribution with peak sizes at 77.2 nm (σ = 17.2 nm) and 25 nm (σ = 25.3 nm) at the laser fluence of 2.6 J/cm^2 shifts to a unimodal distribution with peak size at 17.0 nm (σ = 10.9 nm) for the laser fluence of 10.5 J/cm^2. These results are also

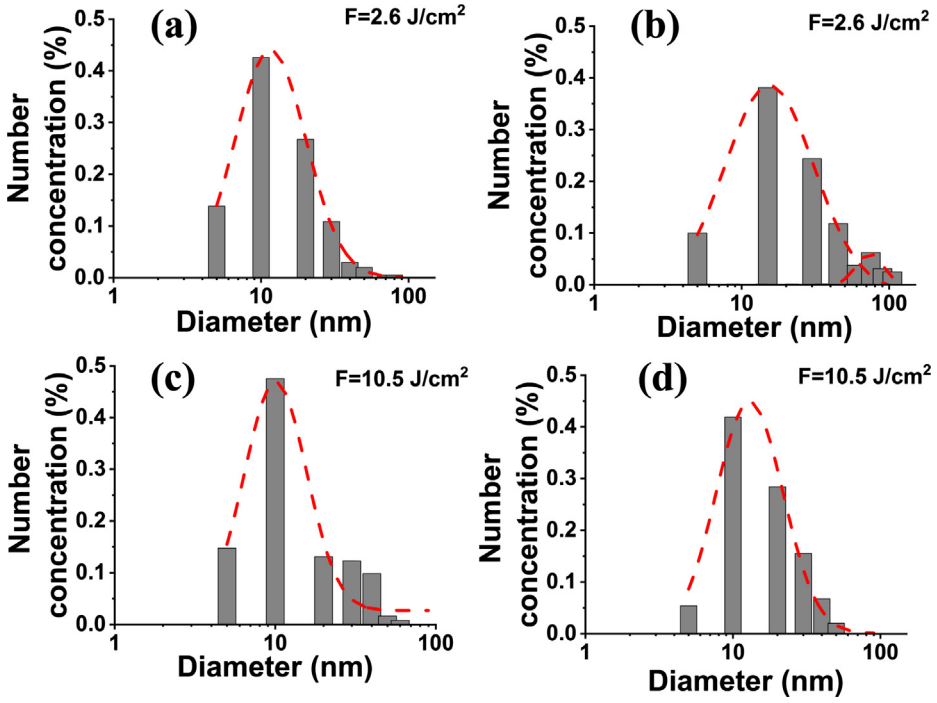

Fig. 7. Effect of laser fluence (F, J/cm^2) on the size distribution of C/Al NPs prepared via LASiS in (a & c) acetone and (b & d) in toluene.

in agreement with previous studies from our group on cobalt nanostructures [60]. The systematic decrease in the particles size can be explained based on the nucleation and formation of primary Al NPs. As the laser fluence increases more Al is ablated, which results in greater Al monomer concentration (n_{Al}). The saturation ratio (S) of Al monomers that encounter gas phase synthesis inside the cavitation bubble is defined as: $S = n_{Al}/n_s$, where n_{Al} is the Al monomer concentration and n_s is the saturated monomer concentration. Therefore, the volume loading and S of Al monomers increase as n_{Al} increases. According to classical nucleation theory (CNT) [61,62], the size of the nucleated primary particles (d^*) is proportional to the inverse of saturation ratio logarithm:

$$d^* = \frac{2\theta}{3\ln(S)}\left(\frac{6v_1}{\pi}\right)^{1/3}$$

where θ is the normalized surface tension of the Al particles and v_1 is the volume of Al monomer. Hence, the increase in the laser fluence results greater saturation ratio and consequently leads to smaller primary particles.

3.2. Energetic characterization

For analyzing the energetic properties of the aforementioned C/Al NP composites, four samples were prepared by ablating the Al target for 4 min under various laser fluxes in acetone or toluene and tested using LASEM. Fig. 8 illustrates the laser-induced shock velocities measured for these samples, as compared to commercial nano-sized energetic Al powders with a native oxide layer. The blank indicates the laser-induced shock velocity for the inert substrate (double-sided tape). Comparing the LASEM results for the laser-induced shock velocities (m/s) from blank substrate (control) to the Al samples, one can immediately notice the increase in the velocities for the Al-containing particles as a result of fast exothermic reactions on the microsecond timescale. The increase in laser-induced plasma temperature due to the exothermic reactions between Al powder and oxygen (either from the sample or air entrained in the plasma) has been previously observed [63]. The current results confirm the ability of the LASEM technique to detect exothermic energetic behavior via laser-induced shock velocity increases from known metal-based energetic material analytes

Moreover, it can be seen that the C/Al NP composites prepared in toluene or acetone show higher characteristic laser-induced shock velocities (> 690 m/s) as compared to the commercial nano-sized Al powder (~670 m/s). In fact the samples prepared in acetone with laser fluences of 2.2 and 2.6 J/cm^2, having peak sizes ~15 nm and relatively narrow size distributions, produce the highest shock velocities (> 755 m/s). One can explain the enhanced energetic behavior

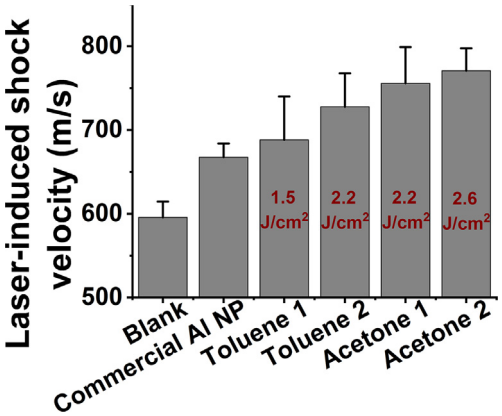

Fig. 8. Comparison of laser-induced shock velocities from LASEM measurements on samples prepared in acetone or toluene at various laser fluences, as compared to commercial nano-Al powders and the blank substrate.

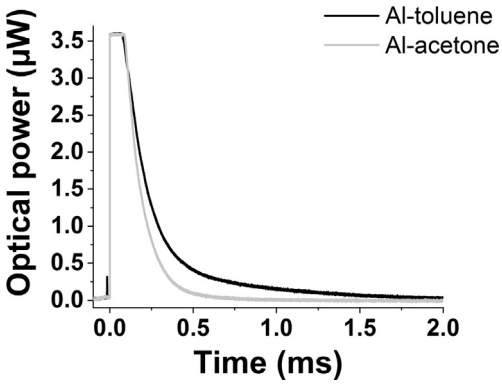

Fig. 9. Time-resolved emission from the reaction of laser-excited C/Al NPs prepared in toluene or acetone.

observed from the synthesized C/Al samples from two perspectives: (1) the protective C/graphitic shells protect the Al NP surfaces from excess oxide layer formation that would hinder the reaction kinetics due to diffusion-limited oxidation pathways through the oxide shell layers; and (2) the earlier onset of pyrolysis in the higher vapor pressure acetone solvent promotes early formation of the amorphous carbon matrix and graphitic structures, dramatically slowing down particle aggregation and thereby generating smaller C/Al NPs (particularly in acetone) which exhibit greater reactivity due to the larger surface area and smaller fuel-oxidizer diffusion length scales. It is well-known from past studies on energetic NPs that as particle sizes decrease, the burning rates and oxidation kinetics become more effective. Here, in the case of the toluene samples, particles show a bimodal size distribution with two modal peaks at 25 nm and 77.2 nm. It is highly likely that the NPs residing at the second peak of 77.2 nm do not undergo complete oxidation on the microsecond-timescale due to the larger sizes and lower surface to volume ratios. Therefore, the bulk of the Al core possibly acts as a dead load during the energy release and retards the energetic reactions. Confirmation of this is the more extensive combustion emission on the millisecond timescale from the C/Al NPs synthesized in toluene (Fig. 9), as compared to the C/Al NPs from acetone that primarily react on the microsecond timescale (as indicated in Fig. 8). While the initial strong emission signal shown in Fig. 9 is a result of the laser-induced plasma emission, combustion of the Al particles following the decay of the plasma appears as a shoulder on this saturated peak. Exothermic reactions that occur later than about 10 μs do not contribute to the laser-induced shock velocity, since at this point in time the shock wave has travelled above the plasma and is only affected by the drag from air.

In a recent study by Gottfried et al. [55], LASEM was effectively employed to correlate laser-induced shock velocity to detonation velocities in order to classify various energetic materials such as TNT (trinitrotoluene), PETN (pentaerythritol trinitrate) etc. as exothermic and/or explosive materials [64]. Upon comparing the LASEM recorded shock velocities from our various C/Al NP composites prepared in toluene and acetone with the known energetic data from the aforesaid study as a function of denotation velocities [64], the C/Al NPs synthesized in toluene clearly indicate exothermic rather than explosive behavior, whereas the samples prepared in acetone fall into the explosive range. However, LASEM estimates of detonation performance assume the material is detonable, and it is not clear how the laser-induced shock velocities of pure metallic samples would correlate to the detonation velocities of organic military explosives [65].

3.3. Oxidative behavior of C/Al NPs: The mechanistic picture

For further investigation into the mechanistic picture behind the excess burning process for the LASiS-synthesized C/Al NPs, Fig. 10 shows the thermo-gravimetric analysis (TGA) for the C/Al sample with

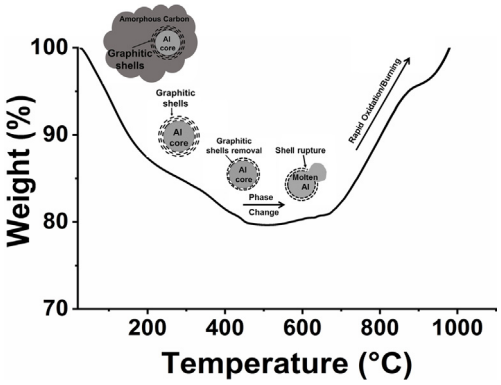

Fig. 10. TGA analysis for the sample with highest LASEM activity (acetone, 2.6 J/cm^2).

the highest LASEM activity (i.e., for samples synthesized in acetone at 2.6 J/cm^2 fluence in Fig. 8). Fig. 10 illustrates thermal decomposition/combustion of the sample in air, by plotting weight as a function of temperature (^{o}C). It can be observed that the sample weight decreases continuously up to ~470 °C. This can be readily explained by the fact that as the amorphous carbon matrix/shell burns, it turns to gaseous by-products such as CO and CO_2 and the sample weight decreases. Between ~470 °C up to ~700 °C the weight does not change drastically, possibly due to phase changes from solid to molten Al prior to the onset of Al oxidation. As also discussed and explained in earlier works for oxide coated Al NPs [66], here the core Al NP melts inside the C shell to generate excess internal pressure due to the large volume expansion which, in turn, ruptures the C shell with relatively lower thermal expansion coefficients. This mechanical rupture releases the highly active and hot molten Al to the oxidizing environment resulting in instantaneous burning/oxidation. Here, one needs to bear in mind that the low young's modulus (~4–30 GPa), high melting point (~3500 °C), and thermal conductivity (~10–114 W/m-K) of graphitic shells play a critical role in heating the encapsulated Al core to its melting point, producing large internal stresses without buckling the shell. Upon reaching a critical activation T and P, such scaffolds typically collapse via melt dispersion or nanoexplosions [67,68] to initiate instantaneous kinetically-driven oxidation of the as-released core nanoclusters. It should be noted that size-dependent Laplace pressure (~surface tension/particle radius) and stress inside such NPs can exceed ambient pressure by many orders of magnitude (~10–20 GPa) [69]. Thus, in the TGA data in Fig. 10, we observe a sudden increase in the sample weight at around ~700 °C. This behavior can be explained by rupture of the remaining graphitic shells between ~470–700 °C and Al oxidation initiation ~700 °C, which consequently increases the sample weight. Previous mass spectrometry studies have also recorded the onset of Al NP oxidation at ~600–700 °C for particle sizes < 50 nm [12]. Added to this, one also needs to bear in mind that while internal pressures inside the shell can rise dramatically for smaller NPs (Laplace pressure effects ~ surface tension/radius) [70], melting points can drop drastically (Tolman effects) [71] – accelerating the phase transition of the Al. In summary, these results are in good agreement with previous studies that have captured similar behavior and temperatures for the oxidation of coated Al NPs [22].

4. Conclusion

LASiS has been employed for synthesizing energetic nanocomposites consisting of graphitic shell coated Al NPs embedded in a carbon matrix. The shell-core C/Al NPs have been prepared through laser ablation in acetone or toluene under various laser fluences. STEM and EELS measurements revealed the size distribution and morphology of the composite C/Al NPs, including the graphitic shell coatings on the Al NP cores. Our results indicate that the size distributions and energetic behavior of the C/Al NPs could be tailored by tuning the LASiS medium (i.e., organic solvent), laser flux and ablation times. The energetic activities of the samples have been tested and compared to a commercial nano-Al powder using LASEM. The results indicate that the samples prepared in acetone or toluene show higher energetic activities as compared to commercial nano-Al powder owing to their smaller sizes and the protective graphitic shell coatings on the Al NPs. Specifically, the C/Al NPs prepared in acetone exhibited higher laser-induced shock velocities as compared to the samples synthesized in toluene, with the samples made from ablation under a laser fluence of 2.6 J/cm^2 indicating the highest activities. Although the C/Al NPs made via LASiS in toluene behave as exothermic materials when compared to their counterparts grown in acetone that exhibit more explosive properties (i.e., react more rapidly), a definitive conclusion on their exothermic/explosive behaviors would demand further investigation into their structure-property characteristics and reaction propagation mechanisms. In addition, refinement of the synthesis process to produce more homogeneously distributed Al NPs with C shells is part of our ongoing research efforts that could provide additional enhancements in the microsecond-timescale energy release. In summary, our work here paves the path for the future design of energetic metal/intermetallic NPs encapsulated in nanostructured graphitic shell coatings and/or fullerene-like layers that can be tailored via LASiS-based techniques to tune their reactive behaviors for a myriad of defense and solid-state propellant applications.

Acknowledgements

Scientific support for this work was provided through the US Army Research Laboratory's (ARL) External Collaboration Initiative (ECI) Award with Dr Jennifer L. Gottfried at the ARL, Aberdeen Proving Ground (APG), Aberdeen, MD.

References

[1] M. Mench, et al., Comparison of thermal behavior of regular and ultra-fine aluminum powders (Alex) made from plasma explosion process, Combust. Sci. Technol. 135 (1–6) (1998) 269–292.
[2] A. Rai, et al., Understanding the mechanism of aluminium nanoparticle oxidation, Combust. Theor. Model. 10 (5) (2006) 843–859.
[3] M.J. Chiaverini, et al., Instantaneous regression behavior of HTPB solid fuels burning with GOX in a simulated hybrid rocket motor, Int. J. Energetic Mater. Chem. Propulsion 4 (1–6) (1997).
[4] J. Renie, et al., Aluminum particle combustion in composite solid propellants, 18th Joint Propulsion Conference, (1982).
[5] N. Bakhman, A. Belyaev, Y.A. Kondrashkov, Influence of the metal additives onto the burning rate of the model solid rocket propellants, Phys. Combust. Explos. 6 (1970) 93.
[6] H. Ritter, S. Braun, High explosives containing ultrafine aluminum ALEX, Propellants Explos. Pyrotech. 26 (6) (2001) 311–314.
[7] A. Ilyin, et al., Characterization of aluminum powders I. Parameters of reactivity of aluminum powders, Propellants Explos. Pyrotech. 27 (6) (2002) 361–364.
[8] P. Brousseau, C.J. Anderson, Nanometric aluminum in explosives, Propellants Explos. Pyrotech. 27 (5) (2002) 300–306.
[9] V. Weiser, S. Kelzenberg, N. Eisenreich, Influence of the metal particle size on the ignition of energetic materials, Propellants Explos. Pyrotech. 26 (6) (2001) 284–289.
[10] L. Zhou, et al., Time-resolved mass spectrometry of the exothermic reaction between nanoaluminum and metal oxides: the role of oxygen release, J. Phys. Chem. C 114 (33) (2010) 14269–14275.
[11] D. Mukherjee, A. Rai, M.R. Zachariah, Quantitative laser-induced breakdown spectroscopy for aerosols via internal calibration: application to the oxidative coating of aluminum nanoparticles, J. Aerosol Sci. 37 (6) (2006) 677–695.
[12] K. Park, et al., Size-resolved kinetic measurements of aluminum nanoparticle oxidation with single particle mass spectrometry, J. Phys. Chem. B 109 (15) (2005) 7290–7299.
[13] M.L. Pantoya, J.J. Granier, Combustion behavior of highly energetic thermites: nano versus micron composites, Propellants Explos. Pyrotech. 30 (1) (2005) 53–62.
[14] A. Pivkina, et al., Nanomaterials for heterogeneous combustion, Propellants Explos. Pyrotech. 29 (1) (2004) 39–48.
[15] R.A. Yetter, G.A. Risha, S.F. Son, Metal particle combustion and nanotechnology, Proc. Combust. Inst. 32 (2) (2009) 1819–1838.
[16] D. Mukherjee, M. Wang, B. Khomami, Impact of particle morphology on surface oxidation of nanoparticles: a kinetic Monte Carlo based study, Aiche J. 58 (11)

(2012) 3341–3353.
[17] E.L. Dreizin, Metal-based reactive nanomaterials, Prog. Energy Combust. Sci. 35 (2) (2009) 141–167.
[18] A. Prakash, A.V. McCormick, M.R. Zachariah, Tuning the reactivity of energetic nanoparticles by creation of a core-shell nanostructure, Nano Lett. 5 (7) (2005) 1357–1360.
[19] K. Sullivan, G. Young, M.R. Zachariah, Enhanced reactivity of nano-B/Al/CuO MIC's, Combust. Flame 156 (2) (2009) 302–309.
[20] A. Prakash, A.V. McCormick, M.R. Zachariah, Synthesis and reactivity of a super-reactive metastable intermolecular composite formulation of Al/KMnO4, Adv. Mater. 17 (7) (2005) p. 900-+.
[21] R.J. Jouet, et al., Surface passivation of bare aluminum nanoparticles using perfluoroalkyl carboxylic acids, Chem. Mater. 17 (11) (2005) 2987–2996.
[22] K. Park, A. Rai, M. Zachariah, Characterizing the coating and size-resolved oxidative stability of carbon-coated aluminum nanoparticles by single-particle mass-spectrometry, J. Nano. Res. 8 (3–4) (2006) 455–464.
[23] S.A. Davari, D. Mukherjee, Kinetic Monte Carlo simulation for homogeneous nucleation of metal nanoparticles during vapor phase synthesis, AIChE J. 64 (1) (2018) 18–28.
[24] D. Mukherjee, S.A. Davari, Computational modeling for fate, transport and evolution of energetic metal nanoparticles grown via aerosol route, Energetic Materials, Springer, 2017, pp. 271–341.
[25] D. Mukherjee, A. Prakash, M.R. Zachariah, Implementation of a discrete nodal model to probe the effect of size-dependent surface tension on nanoparticle formation and growth, J. Aerosol Sci. 37 (10) (2006) 1388–1399.
[26] A. Prakash, A.P. Bapat, M.R. Zachariah, A simple numerical algorithm and software for solution of nucleation, surface growth, and coagulation problems, Aerosol Sci. Technol. 37 (11) (2003) 892–898.
[27] D. Zhang, B. Gökce, S. Barcikowski, Laser synthesis and processing of colloids: fundamentals and applications, Chem. Rev. 117 (5) (2017) 3990–4103.
[28] A.M. Morales, C.M. Lieber, A laser ablation method for the synthesis of crystalline semiconductor nanowires, Science 279 (5348) (1998) 208–211.
[29] W.S. Shi, et al., Laser ablation synthesis and optical characterization of silicon carbide nanowires, J. Am. Ceram. Soc. 83 (12) (2000) 3228–3230.
[30] G.P. Johnston, et al., Reactive laser ablation synthesis of nanosize alumina powder, J. Am. Ceram. Soc. 75 (12) (1992) 3293–3298.
[31] D.P. Yu, et al., Synthesis of boron nitride nanotubes by means of excimer laser ablation at high temperature, Appl. Phys. Lett. 72 (16) (1998) 1966–1968.
[32] A. Ciucci, et al., New procedure for quantitative elemental analysis by laser-induced plasma spectroscopy, Appl. Spectrosc. 53 (8) (1999) 960–964.
[33] S.A. Davari, et al., Calibration-free quantitative analysis of thin-film oxide layers in semiconductors using laser induced breakdown spectroscopy (LIBS), J. Anal. At. Spectrom. 32 (7) (2017) 1378–1387.
[34] D.W. Hahn, N. Omenetto, Laser-induced breakdown spectroscopy (LIBS), Part II: review of instrumental and methodological approaches to material analysis and applications to different fields, Appl. Spectrosc. 66 (4) (2012) 347–419.
[35] S.A. Davari, et al., In-vitro analysis of early calcification in aortic valvular interstitial cells using Laser-Induced Breakdown Spectroscopy (LIBS), J. Biophoton. (2018) 11(1).
[36] S.A. Davari, et al., Detection of interstitial oxygen contents in Czochralski grown silicon crystals using internal calibration in laser-induced breakdown spectroscopy (LIBS), Talanta 193 (2019) 192–198.
[37] V. Amendola, M. Meneghetti, Laser ablation synthesis in solution and size manipulation of noble metal nanoparticles, PCCP 11 (20) (2009) 3805–3821.
[38] D. Mukherjee, S. Hu, Compositions, Systems and Methods for Producing Nanoalloys, and/or Nanocomposites using tandem Laser Ablation Synthesis in Solution-Galvanic Replacement Reaction, 2016, USA.
[39] D.S. Zhang, B. Goekce, S. Barcikowski, Laser synthesis and processing of colloids: fundamentals and applications, Chem. Rev. 117 (5) (2017) 3990–4103.
[40] A. Letzel, et al., Size quenching during laser synthesis of colloids happens already in the vapor phase of the cavitation bubble, J. Phys. Chem. C 121 (9) (2017) 5356–5365.
[41] M.R. Kalus, et al., How persistent microbubbles shield nanoparticle productivity in laser synthesis of colloids – quantification of their volume, dwell dynamics, and gas composition, PCCP 19 (10) (2017) 7112–7123.
[42] V. Amendola, S. Barcikowski, A quarter-century of nanoparticle generation by lasers in liquids: where are we now, and what's next? J. Colloid Interface Sci. 489 (2017) 1–2.
[43] O. Prymak, et al., Crystallographic characterization of laser-generated, polymer-stabilized 4 nm silver-gold alloyed nanoparticles, Mater. Chem. Phys. 207 (2018) 442–450.
[44] G. Marzun, et al., Role of dissolved and molecular oxygen on Cu and PtCu alloy particle structure during laser ablation synthesis in liquids, ChemPhysChem 18 (9) (2017) 1175–1184.
[45] G. Marzun, et al., Size control and supporting of palladium nanoparticles made by laser ablation in saline solution as a facile route to heterogeneous catalysts, Appl. Surf. Sci. 348 (2015) 75–84.
[46] S. Hu, et al., PtCo/CoOx nanocomposites: bifunctional electrocatalysts for oxygen reduction and evolution reactions synthesized via tandem laser ablation synthesis in solution-galvanic replacement reactions, Appl. Catal. B-Environ. 182 (2016) 286–296.
[47] S.A. Davari, S. Hu, D. Mukherjee, Calibration-free quantitative analysis of elemental ratios in intermetallic nanoalloys and nanocomposites using Laser Induced Breakdown Spectroscopy (LIBS), Talanta 164 (2017) 330–340.
[48] S. Hu, et al., Tandem laser ablation synthesis in solution-galvanic replacement reaction (LASiS-GRR) for the production of PtCo nanoalloys as oxygen reduction electrocatalysts, J. Power Sources 306 (2016) 413–423.
[49] S.A. Davari, et al., Rapid elemental composition analysis of intermetallic ternary nanoalloys using calibration-free quantitative Laser Induced Breakdown Spectroscopy (LIBS), MRS Adv. 2 (55) (2017) 3371–3376.
[50] S. Hu, et al., A facile and surfactant-free route for nanomanufacturing of tailored ternary nanoalloys as superior oxygen reduction reaction electrocatalysts, Catal. Sci. Technol. 7 (10) (2017) 2074–2086.
[51] S. Hu, et al., Hybrid nanocomposites of nanostructured Co3O4 interfaced with reduced/nitrogen-doped graphene oxides for selective improvements in electrocatalytic and/or supercapacitive properties, RSC Adv. 7 (53) (2017) 33166–33176.
[52] A. Baladi, R.S. Mamoory, Investigation of different liquid media and ablation times on pulsed laser ablation synthesis of aluminum nanoparticles, Appl. Surf. Sci. 256 (24) (2010) 7559–7564.
[53] R. Kuladeep, et al., Investigation of optical limiting properties of Aluminium nanoparticles prepared by pulsed laser ablation in different carrier media, J. Appl. Phys. 114 (24) (2013) 243101.
[54] G. Viau, et al., Internal structure of Al hollow nanoparticles generated by laser ablation in liquid ethanol, Chem. Phys. Lett. 501 (4–6) (2011) 419–422.
[55] J.L. Gottfried, Laboratory-scale method for estimating explosive performance from laser-induced shock waves, Propellants Explos. Pyrotech. 40 (5) (2015) 674–681.
[56] J.L. Gottfried, T.M. Klapötke, T.G. Witkowski, Estimated detonation velocities for TKX-50, MAD-X1, BDNAPM, BTNPM, TKX-55, and DAAF using the laser–induced air shock from energetic materials technique, Propellants Explos. Pyrotech. 42 (4) (2017) 353–359.
[57] J.L. Gottfried, E.J. Bukowski, Laser-shocked energetic materials with metal additives: evaluation of chemistry and detonation performance, Appl. Opt. 56 (3) (2017) B47–B57.
[58] S. Ibrahimkutty, et al., Nanoparticle formation in a cavitation bubble after pulsed laser ablation in liquid studied with high time resolution small angle x-ray scattering, Appl. Phys. Lett. 101 (10) (2012) 103104.
[59] J. Lam, et al., γ-Al 2 O 3 nanoparticles synthesised by pulsed laser ablation in liquids: a plasma analysis, PCCP 16 (3) (2014) 963–973.
[60] S. Hu, C. Melton, D. Mukherjee, A facile route for the synthesis of nanostructured oxides and hydroxides of cobalt using laser ablation synthesis in solution (LASIS), PCCP 16 (43) (2014) 24034–24044.
[61] S.L. Girshick, C.P. Chiu, Homogeneous nucleation of particles from the vapor-phase in thermal plasma synthesis, Plasma Chem. Plasma Process. 9 (3) (1989) 355–369.
[62] S.L. Girshick, P. Agarwal, D.G. Truhlar, Homogeneous nucleation with magic numbers: aluminum, J. Chem. Phys. (2009) 131.
[63] J.L. Gottfried, Laser-induced plasma chemistry of the explosive RDX with various metallic nanoparticles, Appl. Opt. 51 (7) (2012) B13–B21.
[64] J.L. Gottfried, Influence of exothermic chemical reactions on laser-induced shock waves, PCCP 16 (39) (2014) 21452–21466.
[65] J.L. Gottfried, et al., Estimating the relative energy content of reactive materials using nanosecond-pulsed laser ablation, MRS Adv. (2018) 1–12.
[66] A. Rai, et al., Importance of phase change of aluminum in oxidation of aluminum nanoparticles, J. Phys. Chem. B 108 (39) (2004) 14793–14795.
[67] L. Sun, et al., Plastic deformation of single nanometer-sized crystals, Phys. Rev. Lett. 101 (15) (2008) 156101.
[68] S.F. Son, Encapsulated nanoscale particles and inclusions in solid propellant ingredients, in: V.E. Zarko, A.A. Gromov (Eds.), Energetic Nanomaterials: Synthesis, Characterizations, and Application, Elsevier, 2016.
[69] H. Wang, et al., In situ oxidation of carbon-encapsulated cobalt nanocapsules creates highly active cobalt oxide catalysts for hydrocarbon combustion, Nat. Commun. 6 (2015) 7181.
[70] T. Hawa, M.R. Zachariah, Internal pressure and surface tension of bare and hydrogen coated silicon nanoparticles, J. Chem. Phys. 121 (18) (2004) 9043–9049.
[71] H.M. Lu, Q. Jiang, Size-dependent surface tension and tolman's length of droplets, Langmuir 21 (2) (2005) 779–781.